Article

Low-Energy High-Current Pulsed Electron Beam Surface Treatment on the Tribological Behavior of 17-4PH Steel Produced via Binder Jetting

Lorenza Fabiocchi [1,*], Marco Mariani [1], Andrea Lucchini Huspek [2], Matteo Pozzi [2,3], Massimiliano Bestetti [2] and Nora Lecis [1]

[1] Department of Mechanical Engineering, Politecnico di Milano, via Giuseppe La Masa 1, 20156 Milano, Italy; marco.mariani@polimi.it (M.M.); nora.lecis@polimi.it (N.L.)

[2] Department of Chemistry, Materials and Chemical Engineering "Giulio Natta", Politecnico di Milano, via Luigi Mancinelli 7, 20131 Milano, Italy; andrea.lucchinihuspek@polimi.it (A.L.H.); matteo.pozzi@polimi.it (M.P.); massimiliano.bestetti@polimi.it (M.B.)

[3] Rösler Italiana s.r.l., via Elio Vittorini 10/12, 20863 Concorezzo, Italy

* Correspondence: lorenza.fabiocchi@polimi.it

Abstract: Stainless steel 17-4PH is valued for its high strength and corrosion resistance but poses machining challenges due to rapid tool wear. This research investigates the use of pulsed electron beam surface treatment to enhance the surface properties of components fabricated by binder jetting additive manufacturing. The aim is to improve the tribological performance compared to the as-sintered condition and the H900 aging process, which optimizes hardness and wear resistance. Printed samples were sintered in a reducing atmosphere and superficially treated with an electron beam by varying the voltage and the pulse count. Results showed that the voltage affects the roughness and thickness of the treated layer, while the number of pulses influences the hardening of the microstructure and, consequently, the wear resistance. A reciprocating linear pin-on-disk wear test was conducted at 2 N and 10 Hz. Surface-treated samples exhibited lower coefficients of friction, though the values approached those of aged samples after the abrasion of the melted layer, indicating a deeper heat-affected zone formation. Still, the friction remained lower than that of as-printed specimens. This study demonstrates that optimizing electron beam parameters is vital for achieving surface performance comparable to bulk aging treatments, with significant implications for long-term wear resistance.

Keywords: low-energy; high-current pulsed electron beam; tribology; wear; binder jetting 3D printing; 17-4PH stainless steel

1. Introduction

Metal binder jetting (BJT) is an additive manufacturing (AM) technique enabling the fabrication of intricate metal components by sequential application of a liquid binding agent onto successive layers of metal powder [1]. Following printing, the resultant "green" component—a preliminary structure composed of metal powder particles bonded by the liquid ligand—is subjected to curing to consolidate the binder. Subsequently, debinding removes the binder to a specified degree depending on the furnace atmosphere, and then sintering consolidates the metal particles via heating to near-melting temperatures, resulting in a dense and cohesive metal structure [2,3]. BJT offers substantial advantages in production rate, design flexibility, and the ability to fabricate complex geometries without

the requirement for support structures during the shaping phase, making it well suited for prototyping and high-volume manufacturing applications [4–6].

However, steel parts produced by metal BJT typically exhibit significant surface roughness due to the layer-by-layer deposition method, particularly along the build direction. Surface roughness is influenced by parameters such as powder particle size and distribution, binder deposition accuracy, and sintering conditions [7–9]. As-printed steel parts frequently exhibit average surface roughness (R_a) values between 10 and 35 μm, which may be reduced to as low as 1 to 3 μm through post-processing, contingent on application-specific demands. Effective post-processing is essential to refine surface characteristics and enhance mechanical properties, appearance, and functionality [10–13].

To achieve desirable surface properties, several post-processing methods are employed, including mass finishing techniques [14–16] and electropolishing [17–19]. Mass finishing processes are scalable, economical, and versatile, providing manufacturers with a balance between surface quality, throughput, and cost efficiency. Electropolishing offers significant benefits for enhancing surface smoothness, corrosion resistance, and cleanliness, although it presents limitations regarding cost, material compatibility, and dimensional control.

For selective enhancement of specific component areas, high-energy techniques such as electron or laser beam treatments provide significant efficiency in speed and precision. Notably, Low-Energy High-Current Electron Beam (LEHCEB) technology is a targeted approach utilized for surface modification and thermal treatments [20]. LEHCEB produces pulsed electron discharges up to 30 kV and 25 kA with an average pulse duration of 2.5 μs. The source operates by directing a high-density stream of low-energy electrons onto the material surface, which facilitates controlled superficial modification while minimizing penetration depth and preserving the bulk properties of the material [21,22].

The localized heating enabled by LEHCEB induces rapid surface melting and, under some circumstances, evaporation without adversely affecting sub-surface layers. Usually, LEHCEB allows the formation of a homogenized chemical composition and out-of-equilibrium crystalline structures in the remelted layer. Consequently, LEHCEB is suited for applications requiring surface-specific hardening, alloying, or texturing, as it modifies only the outer or near-surface layers, typically on the micrometer scale. Its non-contact nature reduces contamination, wear, and deformation associated with mechanical processing, while the large area of the beam (50 cm^2) guarantees a high throughput, potentially allowing for industrial-scale applications by achieving rapid surface modifications.

This investigation provides a comprehensive assessment of the microstructural and mechanical performance modifications induced by LEHCEB treatment on binder-jetted 17-4PH stainless steel. Emphasis is placed on the surface hardening effects achieved through rapid melting and solidification, as well as the modulation of surface stresses attributed to phase transformations and heat transfer dynamics.

2. Materials and Methods

2.1. Manufacturing and Surface Finishing

17-4PH stainless steel parts were 3D printed with a Desktop Metal Shop System BJT machine by an external supplier (Aidro Srl, Taino, Italy). The feedstock employed was a gas-atomized powder with a D_{90} ~50 μm; thus, the layer thickness was set at 75 μm to avoid single particles exceeding powder bed height. After printing, the powder bed was cured in an air furnace at 180 °C for 6 h to allow the polyethylene glycol-based binder to polymerize and strengthen the green components. The parts were extracted from the loose powder by a combination of manual brushing and compressed air. A single cycle of debinding and sintering above 1300 °C was conducted in a slightly reducing atmosphere (97%Ar/3%H$_2$), effectively removing most of the organic binder and enabling adequate

densification of the material while also minimizing surface oxidation [3,23]. Following sintering, the specimens underwent an H900 aging treatment at 480 °C for 1 h, preceded by a solution annealing cycle at 1050 °C for 1 h [24]. To limit oxidation, both treatments were performed consecutively in a low-vacuum atmosphere, with rapid cooling assisted by an inlet gas flow (N_2). The obtained microstructure (Figure 1) comprises a main martensitic phase, surrounded by delta ferrite formed at high temperatures and inclusions as niobium carbides, especially at the grain boundary, as observed in the literature as well [25–27]. Copper precipitates can be detected only by higher-resolution techniques.
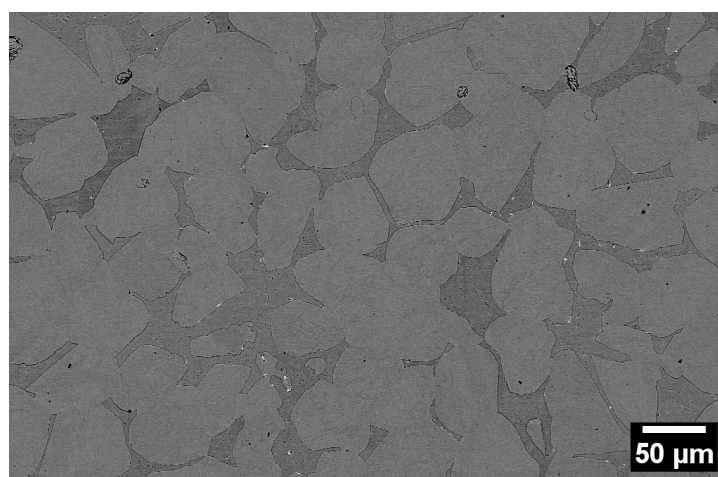
Figure 1. SEM image of an etched section of an as-sintered microstructure.

The surface treatment using LEHCEB was performed in a RITM-SP facility (Microsplav OOO, Tomsk, Russia). Irradiation was carried out at a pressure of 1.8×10^{-4} torr with argon as a working gas. Tests involved three accelerating voltages—20, 25, and 30 kV—corresponding to energy densities of 2.5, 3.3, and 4.9 J cm^{-2}, respectively. A total of 20 and 40 pulses, with an average duration of 2.5 μs, were applied at a repetition frequency of 0.2 Hz. Samples are nominated by the voltage applied and the number of pulses: 20–20, 25–20, 30–20, 20–40, 25–40, and 30–40. After LEHCEB irradiation, samples were allowed to cool in an Ar-saturated environment within the vacuum chamber for 45 min to prevent oxidation.

2.2. Material Characterization

The microstructure of printed and surface-treated components was studied both on the external surface and along the cross-section by scanning electron microscopy (SEM) through a secondary electrons detector equipped with energy dispersive X-ray (EDX) analysis and electron backscattered diffraction (EBSD). The latter images were elaborated by the Tango module in the HKL CHANNEL5 software. Kernel average misorientation (KAM) images were obtained by applying a 3×3 filter size and 5° for subgrain angle in local misorientation value (between 0 and 10) maps. Cross-sections were cut, ground, and polished according to standard metallographic procedures; phase distributions were revealed by etching with a Kalling I reagent. The layer thickness was measured by image analysis on SEM pictures processed through the software ImageJ (version 1.54f) and adopting the line method: eight lines of measurement were taken for each sample.

Surface roughness was measured following the ISO 21920 standard over a measuring length of 4.8 mm with a 0.8 mm cut-off with a contact profilometer [28]. The test was repeated five times to determine the repeatability of the measurement and the homogeneity of the component's surface.

Microhardness was evaluated using a Vickers indentation test, applying a load of 300 gf for 15 s. Tribological performance was tested using an RTEC tribometer in a linear reciprocating pin-on-disk setup. An alumina ball served as counter material, and a 2 N load was applied throughout all tests. The reciprocating movement was set to 10 Hz frequency and maintained for a duration of 10 min. Scratch test was performed on the treated surface by using a Rockwell C indenter of 200 μm diameter. The load varied between 0.3 N to 30 N with a linear increment along the scratch length of 3 mm, with the indenter moving at constant velocity (1.2 mm min^{-1}). Penetration depth and residual depth were taken into account in this analysis: the former is the depth of the material measured during the application of the load; the latter is that measured after the release of the load at the end of the test.

3. Results

3.1. Surface Morphology

In Figures 2–4, the SEM images of the surface morphology are presented at different magnifications to highlight the typical aspect of printed components and the differences generated by the LEHCEB treatment. The H900 (Figure 2c,d) sample has the same surface finishing of the as-sintered ("As is"—Figure 2a,b) component. Indeed, the aging temperatures (1080 °C and 480 °C) are insufficient to promote volume diffusive mechanisms that might alter the peaks and valleys distributions, and the treatment atmosphere employed (low vacuum + N_2) prevents any oxidation or other degradation processes. The surface-treated samples show a smoother aspect by increasing the voltage of the treatment, especially above 25 kV. Regardless of the number of pulses, the uneven roughness owing to the layerwise printing process and the superficial porosity retained within adjacent particles is still clearly visible at 20 kV. Voids are completely removed already at 25 kV, thus suggesting the occurrence of extensive rearrangement of the surface mass thanks to the formation of a liquid fraction.
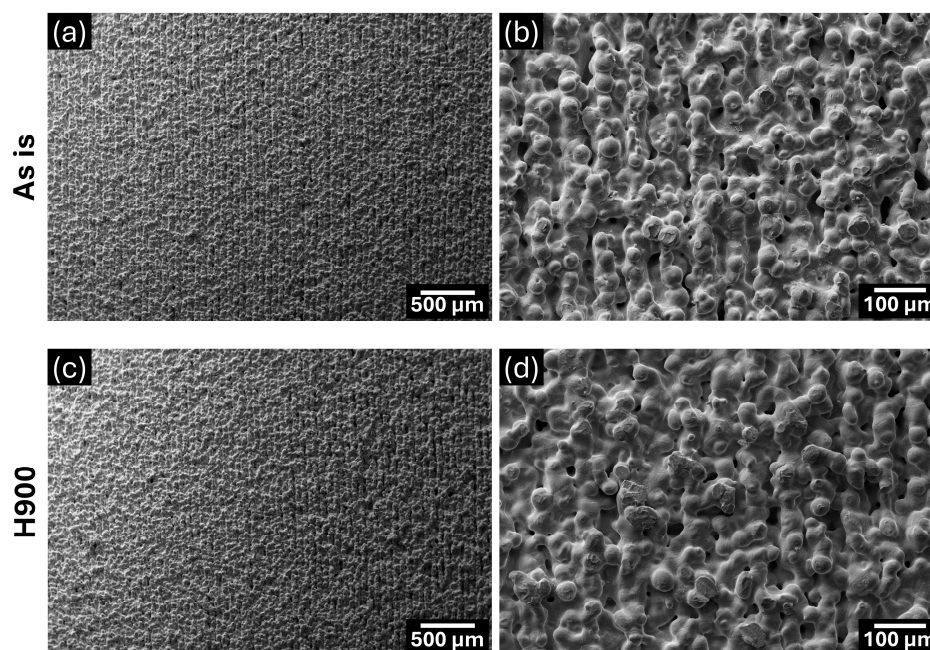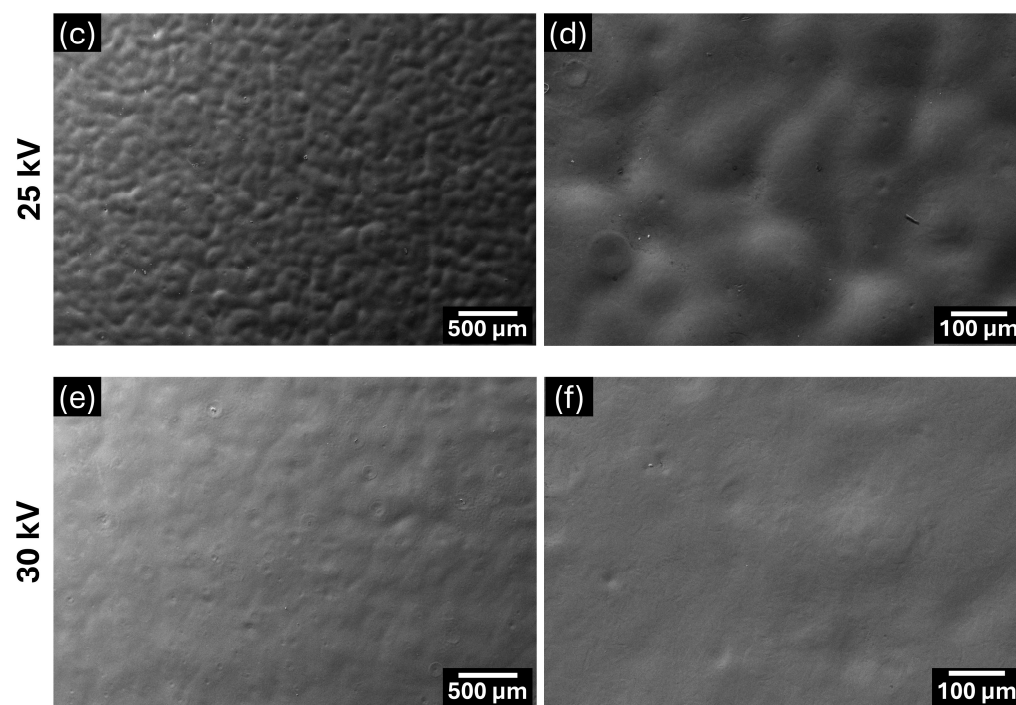

Figure 2. SEM images of as-sintered (**a**) and (**b**) and H900 (**c**) and (**d**) surface morphology.
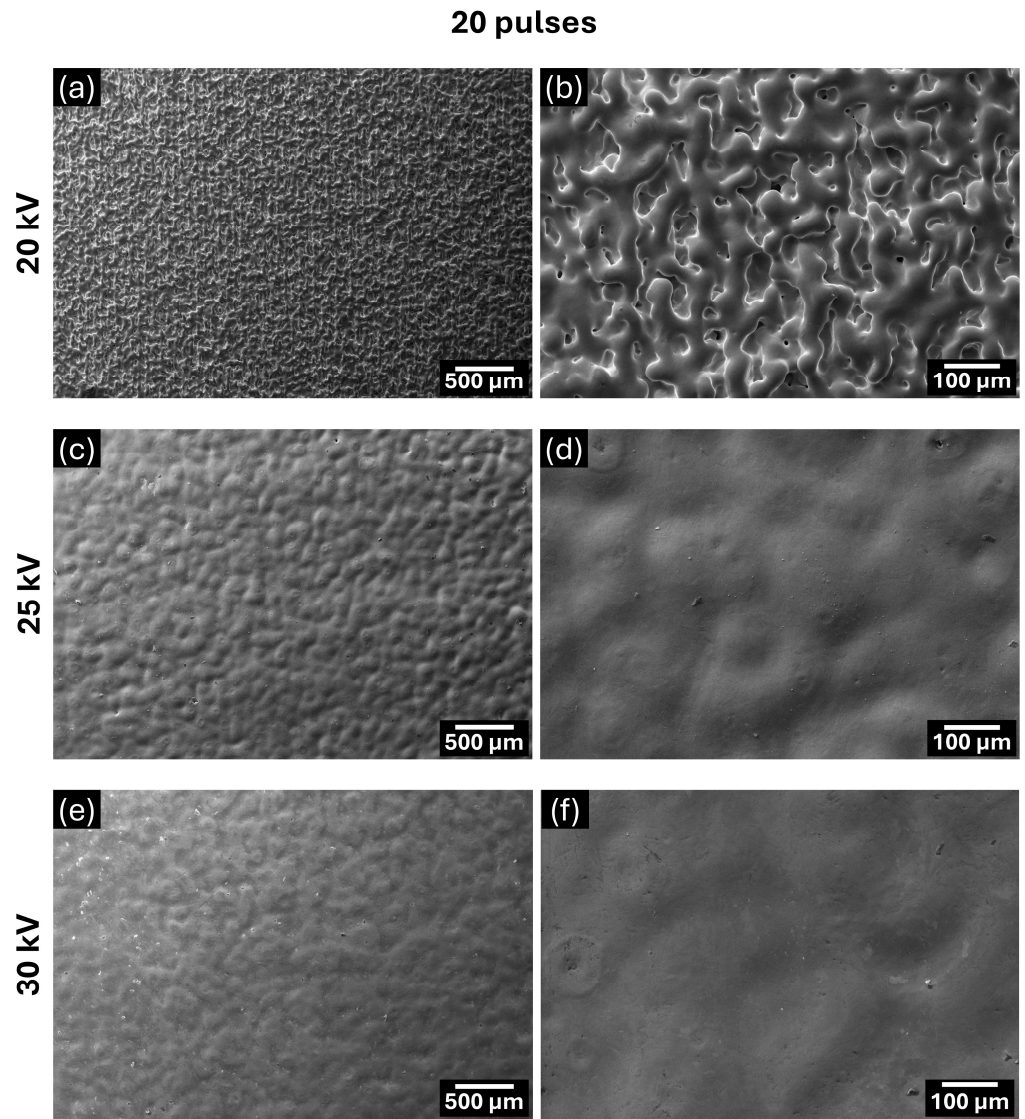
20 pulses

Figure 3. SEM images of 20 pulses surface-treated samples: 20 kV (**a**) and (**b**), 25 kV (**c**) and (**d**), and 30 kV (**e**) and (**f**).
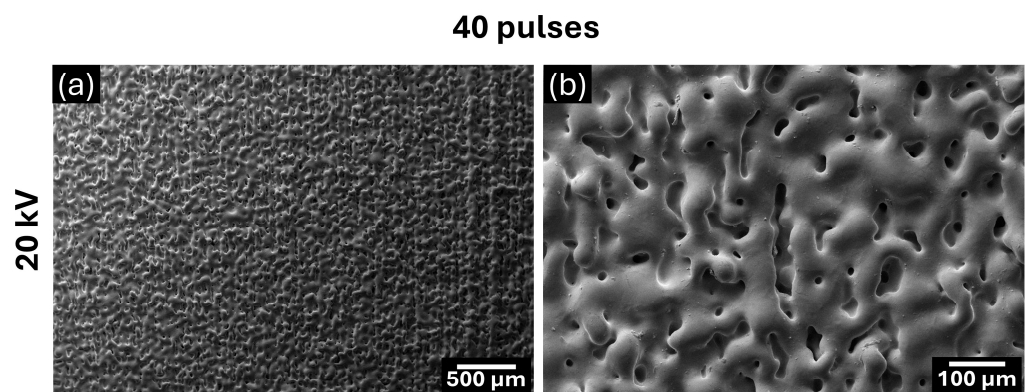
40 pulses

Figure 4. *Cont.*

Figure 4. SEM images of 40 pulses surface-treated samples: 20 kV (**a**) and (**b**), 25 kV (**c**) and (**d**), and 30 kV (**e**) and (**f**).

The roughness measured in the x and y directions (i.e., perpendicular to the building axis) is reported in Figure 5. Statistically significant distinctions among the two planar directions are not observed. The 20 kV surface-treated specimens have comparable roughness to the as-sintered sample, while the 25 kV and 30 kV surface-treated samples have lower roughness independently of the number of pulses used. Higher energy inputs (30 kV, 40 pulses) result in R_a values below 2 μm.
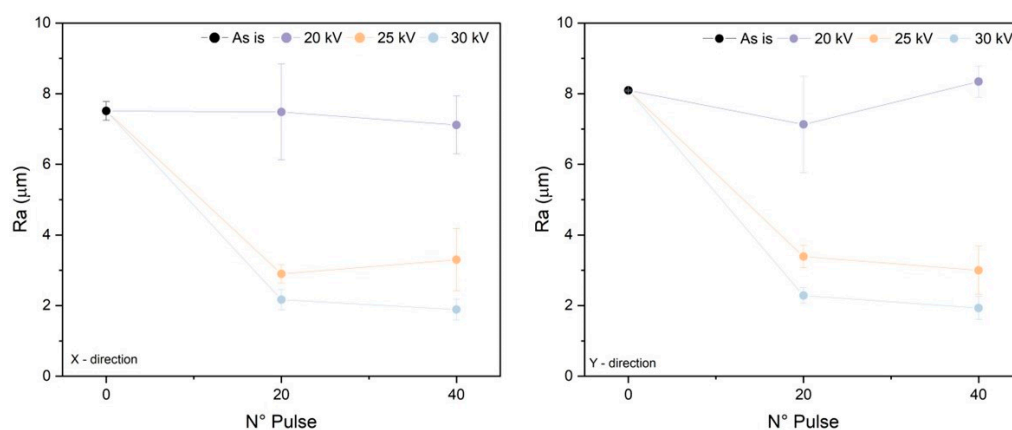
Figure 5. Average roughness measured in the x and y directions with respect to the LEHCEB parameters employed.

3.2. Surface Microstructure

In Figures 6 and 7, the thickness and the morphology of the surface-treated layer are highlighted for the 20 pulses and for the 40 pulses samples, respectively. The average thickness of the LEHCEB-generated layer of each specimen is reported in the graph in Figure 8. Similarly to the results obtained for the surface roughness, the effect of surface finishing becomes particularly relevant for voltages ≥25 kV, regardless of the number of pulses.
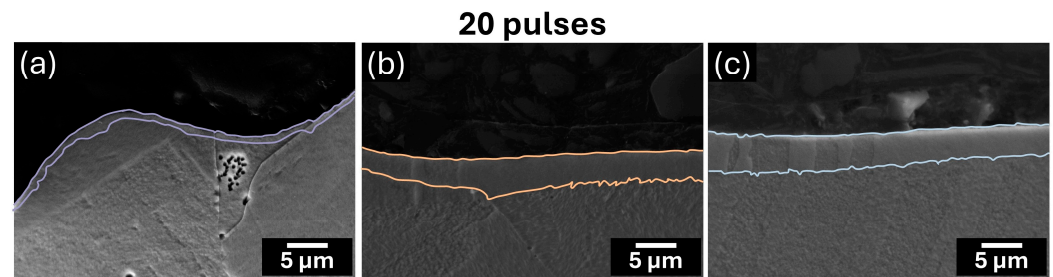
20 pulses

Figure 6. Scanning electron microscopy of the cross-sections of the 20 pulses samples: 20 kV (**a**), 25 kV (**b**), and 30 kV (**c**).
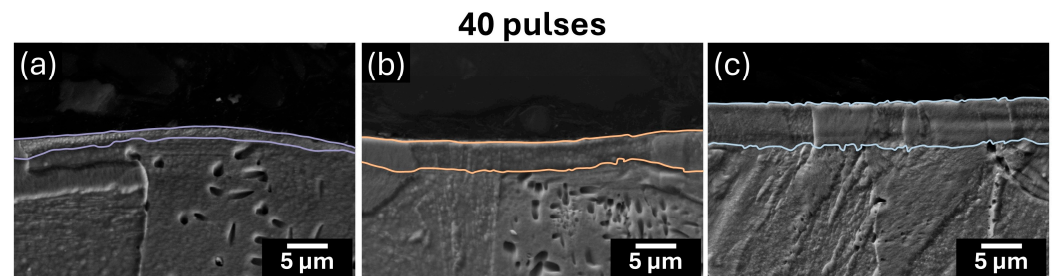
40 pulses

Figure 7. Scanning electron microscopy of the cross-sections of the 40 pulses samples: 20 kV (**a**), 25 kV (**b**), and 30 kV (**c**).
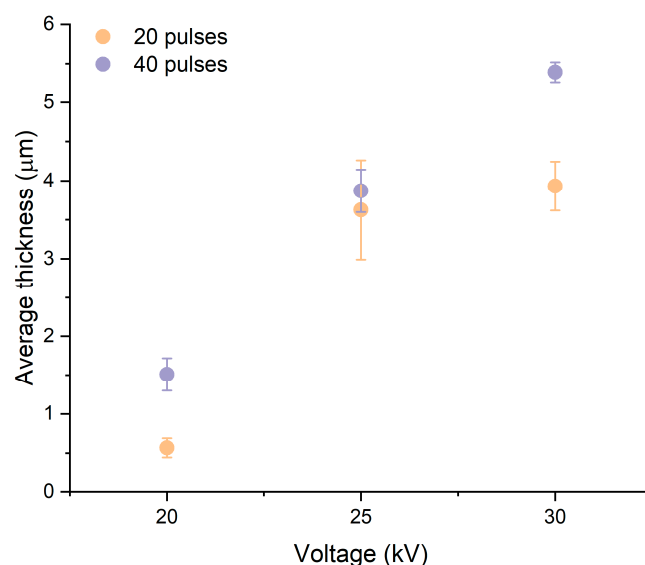
Figure 8. Average thickness of the LEHCEB-generated surface layer measured by image analysis on SEM metallographies.

The effect of the LEHCEB treatment and the consequent modification of the surface and sub-surface regions are affecting phases and grain distribution as well. The difference between the low power (20 kV) and the high power (30 kV) treatments stands in the extension of the liquid fraction generated, thus in the formation of a well-defined layer affected by a recrystallization process upon solidification in the latter case, which leads to the nucleation and epitaxial growth of columnar martensitic and ferritic grains perpendicular to the surface plane, as can be clearly observed in the EBSD images in Figure 9 of the samples "30–20" and "30–40" [21,29]. The characteristic width of these newly formed grains ranges from 1 to 3 μm; therefore, multiple adjacent grains share their surface boundaries with a common grain in the sub-surface region. Therefore, they tend to share the same crystallographic orientation as well, as can be seen in the Euler angles orientation EBSD

pictures. It can be observed that the epitaxial growth occurs regardless of the substrate being a δ ferrite or a martensite grain. The recrystallization process leads to the formation of an ordered microstructure affected by low residual stresses, as highlighted by the KAM signal. Indeed, the signal peaks in the pre-existing martensitic grains and at the high-angle grain boundaries both within and below the melted layer.
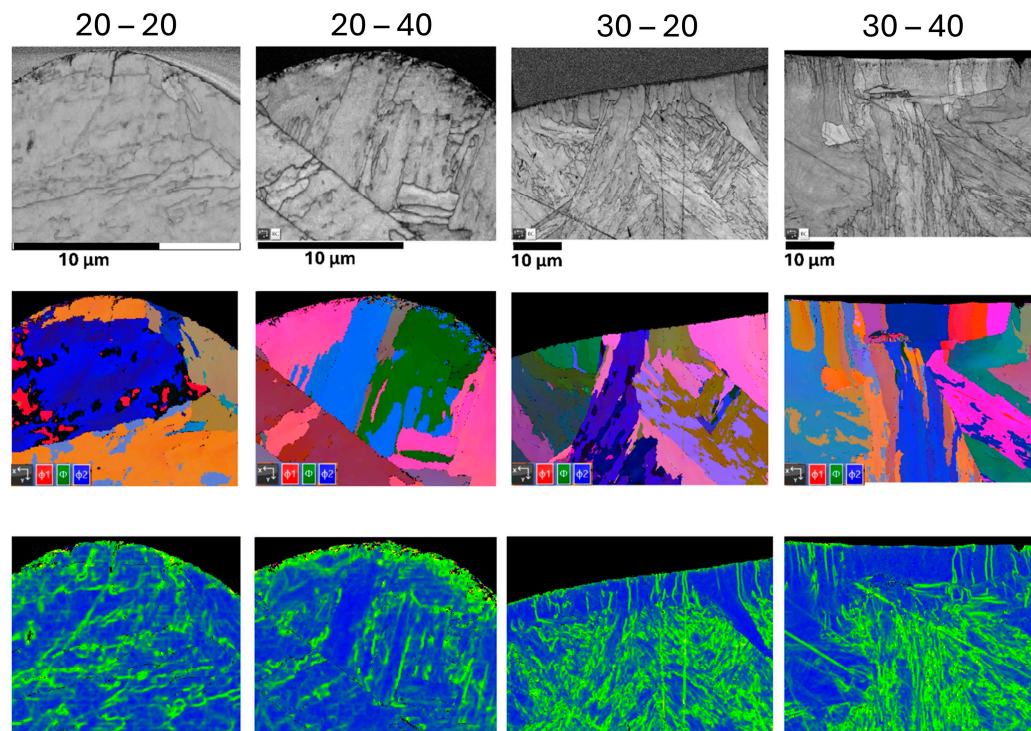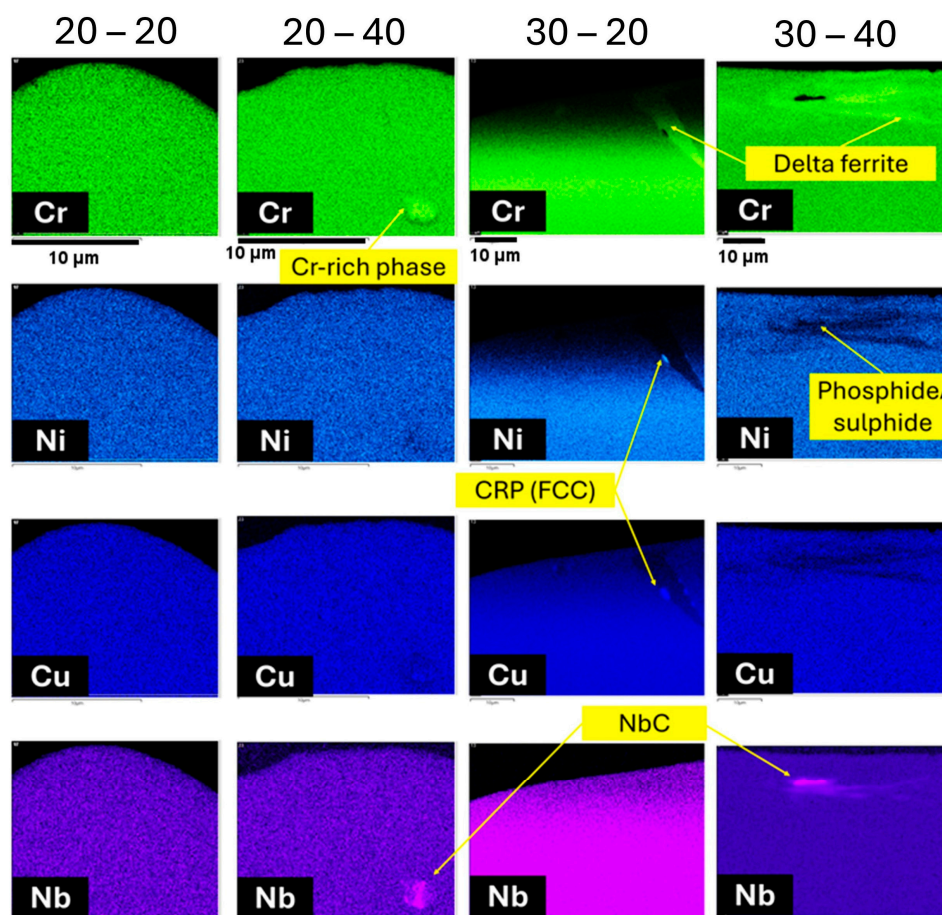

Figure 9. EBSD analysis of selected samples ("20–20" is 20 kV, 20 pulses; "20–40" is 20 kV, 40 pulses; "30–20" is 30 kV, 20 pulses; "30–40" is 30 kV, 40 pulses) cross-sections. From top to bottom: band contrast images, all Euler angles orientation images, and KAM.

The low-power treatment visibly affects only a sub-micrometric depth of the surface without the formation of new grains with a well-determined orientation. It can be expected that the transferred energy is not capable of locally increasing the temperature above the liquidus line; thus, the microstructure is modified by volume diffusion processes alone, especially at grains and α' unit boundaries. The absence of a recrystallization process able to macroscopically rearrange the grains at the surface region implies that the tension generated during the LEHCEB process by the thermal gradient cannot be relieved. In this case, the KAM signal is maximum in correspondence with the surface (see Figure 9 of the samples "20–20" and "20–40").

It can be observed that the temperature increase at the surface is not sufficient to fuse niobium carbides, which have a higher melting point with respect to main phases, as detected in the "30–40" sample (Figure 10). Consequently, they might be trapped at the solid–liquid interface during the treatment and act as a preferential nucleation site for additional inclusions, such as phosphide, sulfides, and Cr- and Cu-rich phases (CRP), thanks to the high mobility of the atoms in the liquid phase [30].

Figure 10. EDX analysis of selected samples ("20–20" is 20 kV, 20 pulses; "20–40" is 20 kV, 40 pulses; "30–20" is 30 kV, 20 pulses; "30–40" is 30 kV, 40 pulses) cross-sections. From top to bottom: chromium, nickel, copper, and niobium content.

3.3. Scratch and Wear Testing

In Figure 11, the different morphology of the scratches on the different surface-treated samples is presented. It can be noticed that the profile of the track is more regular for samples treated at 30 kV, regardless of the load progressive variation during testing. The 20 kV-treated samples feature track contours with low uniformity, especially when the applied load is reduced below 1.5 N, and becomes almost undetectable for loads <0.75 N. In such cases, only the peaks of each printed layer are deformed by the indenter tip, whereas the valleys are sufficiently deep to remain unaltered.

Considering the inhomogeneity of the scratch tracks for the low-voltage-treated samples owing to the high surface roughness, the depth of penetration and the residual depth were considered only for the 30 kV samples (Figure 12). The residual deformation was calculated by subtracting the residual depth (i.e., the depth of the track after the release of the indenter) from the penetration depth (i.e., the depth of the track with the applied load). Therefore, these data can account for two possible mechanisms [22]:

- The recovery of the elastic deformation of the material;
- The deformation of the material owing to pre-existing residual stresses, which are relieved by removing a portion of the surface layer.

Thus, this test can provide insight into the mechanical behavior of the accumulated stress in the steel region under the surface-treated layer. It can be noted that the 30–20 sample has a larger residual deformation than the 30–40 for the entirety of the scratch track length, thus regardless of the applied load.
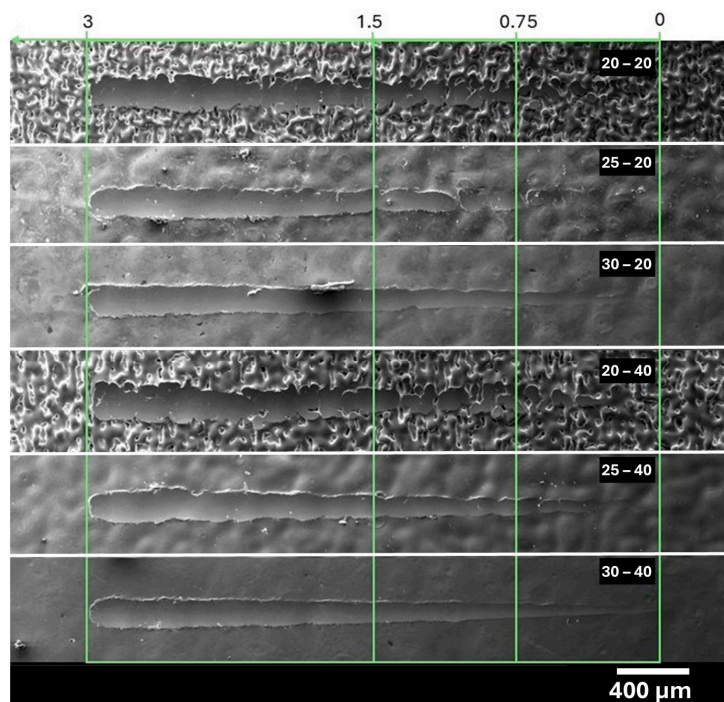
Figure 11. Scanning electron microscopy of the scratch test tracks on LEHCEB-treated samples. Reference load values are indicated at the top of the image. Samples are identified by 4 digits: the first two refer to the voltage applied, and the latter to the number.
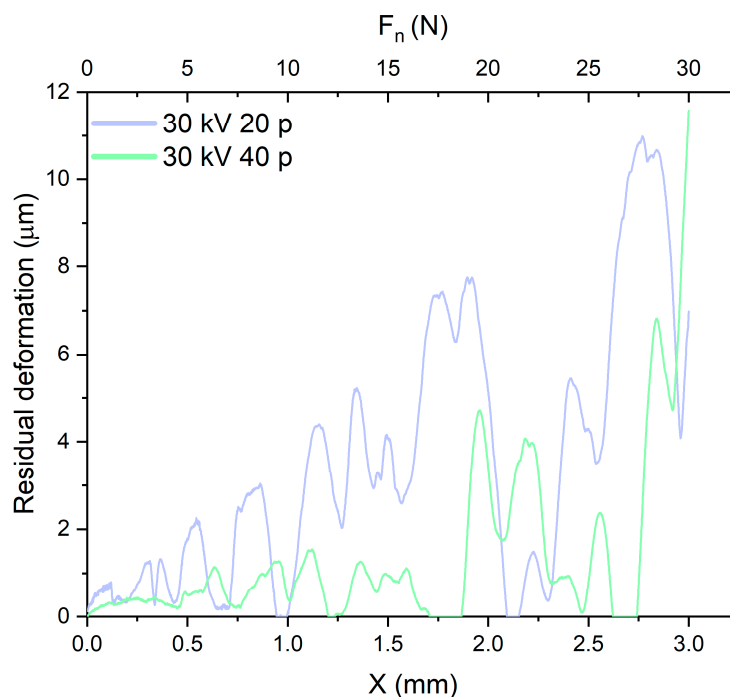
Figure 12. Calculated residual deformation in function of scratch distance and load of the 30 kV samples.

The friction coefficient curves of the different surface-treated samples are reported in Figure 13 and compared to one of the as-sintered and H900 thermally treated samples.

The as-sintered sample (black line) is the only case presenting an increasing COF for the whole duration of the wear test. Differently from the H900 sample (red line), the surface finished materials have two stages in the friction coefficient curve. In the first, the measured value is low and stable at about 0.1; then, it experiences a sharp increase after

a traveled distance strictly dependent on the LEHCEB parameters, finally stabilizing at values between 0.4 and 0.6.
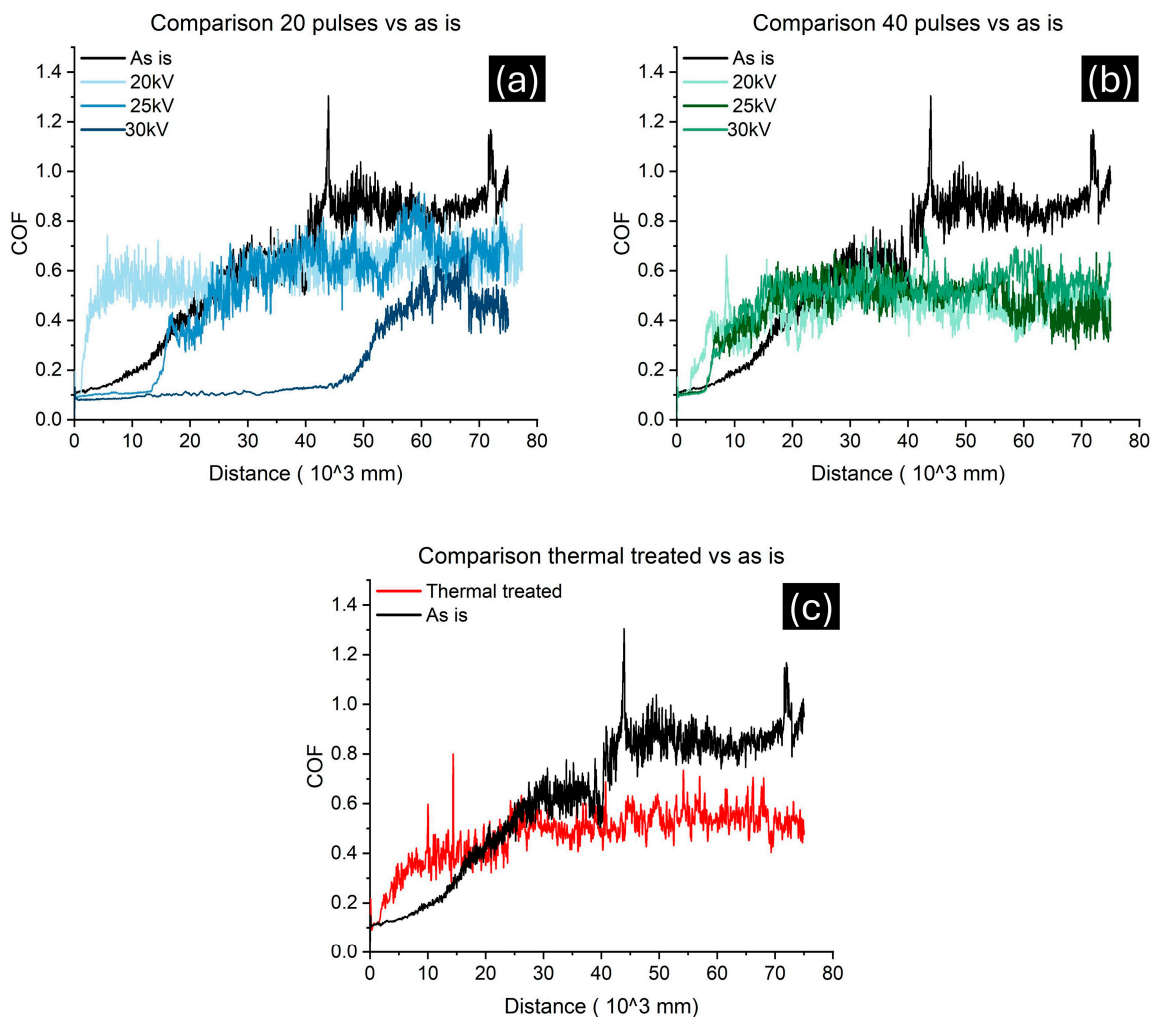
Figure 13. Friction coefficient vs. traveled distance measured during the wear test: 20 pulses (**a**), 40 pulses (**b**), and thermal-treated H900 (**c**) compared to the as-sintered ("as is").

It can be observed that the first part of the COF curve has a low and stable friction coefficient of considerable duration only for the 20 pulses LEHCEB samples, whereas the 40 pulses are rapidly subject to the transient to higher COF even in the case of 25/30 kV. The second plateau reached is stabilized at values comparable to the H900 one, well below the curve obtained from the as-sintered surface. Thus, it can be stated that the LEHCEB treatment alters the mechanical performance of the surface layer as well as the sub-surface region, which experiences an improvement comparable to that achieved by controlled precipitation hardening of coherent copper phases.

Wear tracks of the surface-treated sample are reported in Figure 14 and compared to one of the as-sintered and thermal-treated ones. Distinct distributions of wear are visible between the studied samples. Differently from scratch tracks, the regularity and the depth of the wear tracks not only depend on the voltage applied but also on the number of pulses. Indeed, it can be observed that lower voltages are associated with deeper tracks in the case of 20 pulses, but this is not the case for 40 pulses. It can be noticed that the surface treated with 30 kV and 40 pulses displays a deep and distributed track.
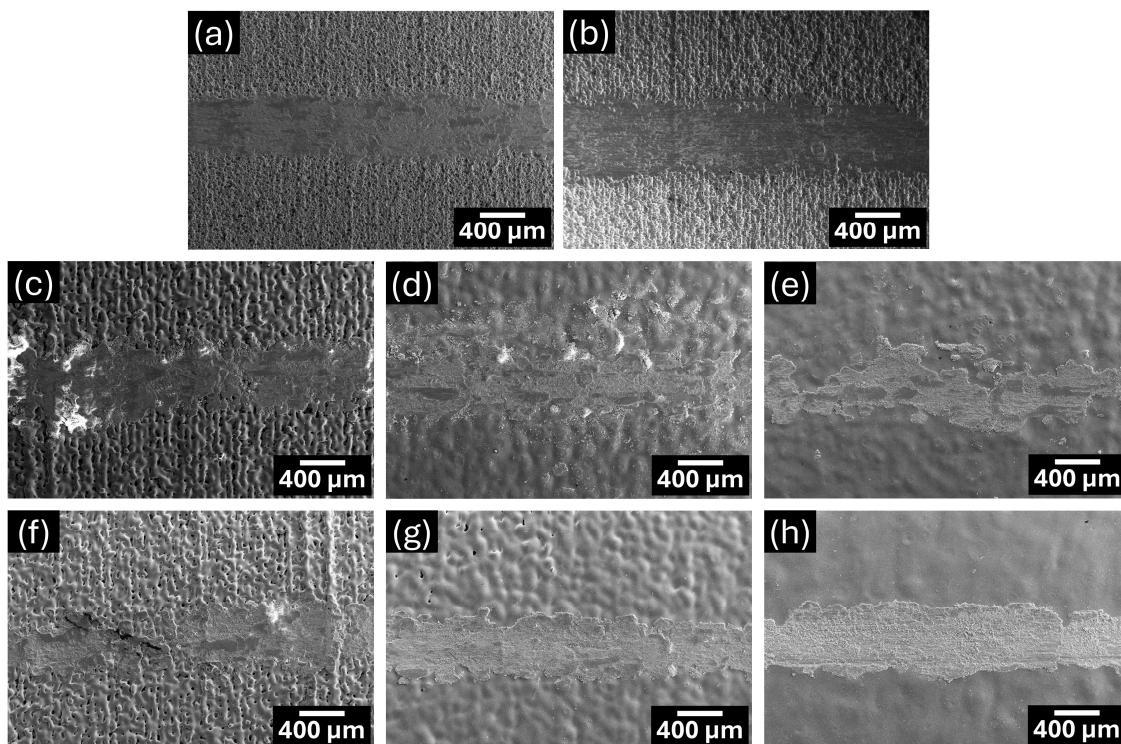
Figure 14. Scanning electron microscopy of wear tracks on as-sintered (**a**), H900 (**b**), and LEHCEB-treated samples: 20–20 (**c**), 25–20 (**d**), 30–20 (**e**), 20–40 (**f**), 25–40 (**g**), and 30–40 (**h**).

4. Discussion

As-sintered and thermally aged H900 samples have identical surface morphologies generated by the fabrication process, influenced by the powder dimension and the layerwise deposition method. Moreover, the thermal treatment does not affect the surface roughness. For this reason, in Figure 5, only the roughness of the as-is sample is considered and compared to the one of the surface-treated samples.

Regarding the samples that underwent the surface treatment with the same number of pulses, it was observed that the surface smoothed and the roughness decreased by increasing the acceleration voltage of the electron beam: higher energies transferred to the sample surfaces promote the local increase in temperature, which is responsible for the formation of a larger liquid fraction. Consequently, the fused material fills the porosity of the surface and facilitates the redistribution of mass from the peaks to the valleys thanks to capillary pressure. The roughness difference between the sample treated at 20 kV and 25 kV is higher compared to the difference between the one treated at 25 kV and 30 kV: for voltages $\geq$ 25 kV, the liquid fraction generated is consistently larger than that at 20 kV and the mass redistribution achieved in the time interval of the surface treatment is comparable.

It appears that the roughness and surface morphology do not change much between the samples treated with the same acceleration voltage but different numbers of pulses. The temperature achieved during the treatment is constant at each pulse; thus, the liquid fraction generated at each pulse does not increase: by increasing the number of pulses, we should expect a similar smoothening effect, which is proportional to the liquid fraction generated. Similarly, the thickness of the resolidified layer depends primarily on the acceleration voltage used, and it is slightly influenced by the number of pulses adopted.

Nonetheless, the repeated transfer of thermal energy to the sub-surface region associated with the number of pulses applied is responsible for a variation in the mechanical properties of the surface portion, comprising both the microstructurally modified surface volume and the region beneath such layer, which can be considered a heat-affected zone.

During the surface treatment with the electron beam, the surface of the material undergoes melting and successively very fast cooling. The cooling rate leads to the refinement of the martensitic microstructure with a columnar grain growth perpendicular to the surface itself. The heat-affected zone is heated for brief intervals of time to temperatures that are insufficient to induce a complete austenitization of the material (>1000 °C), as can be deduced from the fact that the original grains morphology and distribution of the bulk material is retained. Nonetheless, the temperature is sufficiently high to promote the initial formation of copper precipitates, especially coherent ones typical of low-temperature aging (e.g., H900) [22,31].

The influence of the acceleration voltage and the number of pulses is well enlightened by the friction coefficient curves in Figure 13. By increasing the voltage of the surface treatment, there is an increase in the duration of the first stable stage of the COF, showing that higher voltages have a good effect on the wear properties of the material. The effect of the columnar structure of martensite with a perpendicular orientation with respect to the pin direction of motion, together with the overall grain refinement, helped improve the wear resistance of the specimen within the treated layer [21]. The samples treated with an acceleration voltage of 20 kV suffer from an almost immediate transition toward higher COF values because the energy flux of the beam was insufficient to melt or to affect a significantly deep portion of the material. However, the heat generated at the surface was sufficient to perform localized heat treatment on the surface, refining the martensitic sub-units and probably also nucleating new copper precipitates. This heat treatment allowed the layer to resist wearing for a shorter time compared to the higher-voltage sample; however, it was sufficient to improve the friction properties compared to the bare surface of the as-sintered and H900 samples.

The heating effect of the electron beam seems to also have an effect on the sub-surface region of the material. Indeed, the second stage of the COF curves stabilized at a lower value compared to the as-sintered material, closer to that of the H900-aged specimen.

The use of a higher number of pulses for performing the heat treatment causes a deterioration of the wear properties. For higher voltages (25 and 30 kV), the wear resistance of the treated layer was shortened compared to the corresponding samples treated for a lower number of pulses: the transition to the second stage of COF, in fact, occurred seven times faster for the sample treated with 30 kV and almost three times faster for the one treated with 25 kV. The difference at 20 kV and different pulses is less marked since the depth of the directly treated layer is minimal regardless of the number of pulses. Actually, the KAM images in Figure 9 suggest that the layer of the sample treated with 40 pulses presents more high-angle grain boundaries and higher dislocation concentrations, justifying the delayed onset of the second stage of the COF graph compared to the 20 pulses one [32].

Finally, the number of pulses seems to also influence the region below the surface layer of the samples. In fact, although the recrystallized/treated layers have similar thicknesses/microstructures and the sub-surface region is consistent across testing conditions, the specimens treated for 40 pulses display an improvement in the COF value at the second stage of the test. This is coherent with the occurrence of precipitation hardening induced by the heat transferred from the surface by conduction in the sub-surface region. More pulses prolong the duration of thermal aging, leading to increased nucleation of copper precipitates, thus a hardening of the material and an improvement in the wear resistance.

5. Conclusions

This study aimed to evaluate the feasibility of low-energy, high-current electron beam (LEHCEB) surface treatment as a method to enhance the surface properties of binder-jetted components at the as-sintered 17-4PH state. The investigation focused on the effects of

acceleration voltage and the number of pulses on surface morphology, roughness, and wear resistance.

Considering the surface morphology, the layer treated with the electron beam resulted in smoother surfaces, with roughness decreasing as the acceleration voltage increased. This effect was attributed to the higher energy transfer at higher voltages, leading to increased local melting, mass redistribution, and porosity filling. Conversely, the influence of the number of pulses on roughness was less pronounced, as the liquid fraction generated during treatment remained consistent for each pulse.

The microstructure and the thickness of the layer were found to be dependent on the acceleration voltage, while the number of pulses slightly influenced the second one. At lower voltages, the thickness is small and not uniform, whereas the 30 kV-treated samples had a higher thickness with a homogeneous depth and a columnar microstructure determined by the rapid solidification process.

The influence of the acceleration voltage on the tribological properties of the treated layer improved the refining of the martensitic microstructure and induced the formation of copper precipitates, which enhanced hardness and frictional stability in the sub-surface region. The COF curves revealed that samples treated at 25 kV and 30 kV exhibited prolonged wear resistance compared to those treated at 20 kV. However, increasing the number of pulses for higher voltages led to earlier deterioration of wear resistance, likely due to thermal overstressing of the treated layer. For lower voltages (20 kV), the effect of pulse number on wear resistance was less pronounced.

The thermal effects of the electron beam extended to the sub-surface region, promoting precipitation hardening through copper nucleation. While the treated layers exhibited similar thicknesses and microstructures at 30 kV regardless of the number of pulses, the wear analysis indicated that the number of pulses strongly influenced the sub-surface region. Specifically, higher pulse counts negatively impacted tribological properties, as confirmed by the scratch test results and residual depth measurements. This suggests that prolonged thermal exposure during treatment can induce changes in the sub-surface region that deteriorate wear resistance despite the surface layer consistent characteristics.

Overall, the results demonstrate that electron beam surface treatment is a feasible method for improving surface and sub-surface properties. However, the process requires careful optimization of voltage and pulse parameters to balance surface smoothing and wear resistance without causing thermal degradation.

Future studies should focus on optimizing process parameters for specific applications, particularly exploring how pulse count affects sub-surface properties and the long-term tribological behavior of treated materials.

Author Contributions: Conceptualization, M.B. and N.L.; methodology, M.M. and A.L.H.; software, A.L.H.; validation, L.F., M.M. and A.L.H.; formal analysis, L.F., M.M. and A.L.H.; investigation, L.F., M.M., A.L.H. and M.P.; resources, M.B. and N.L.; data curation, L.F.; writing—original draft preparation, L.F., M.M. and A.L.H.; writing—review and editing, M.P., M.B. and N.L.; visualization, L.F. and M.M.; supervision, M.B. and N.L.; project administration, M.B. and N.L.; funding acquisition, M.B. and N.L. All authors have read and agreed to the published version of the manuscript.

Data Availability Statement: The data presented in this study are available on request from the corresponding author due to legal reasons.

Conflicts of Interest: The authors declare no conflict of interest.

References

1. Mariani, M.; Lecis, N.; Mostafaei, A. Binder Jetting-based Metal Printing. In *Solid-State Metal Additive Manufacturing: Physics, Processes, Mechanical Properties, and Applications*; Yu, H.Z., Tuncer, N., Feng, Z., Eds.; John Wiley & Sons Inc.: Hoboken, NJ, USA, 2024; pp. 339–360.

2. Cabo Rios, A.; Olevsky, E.; Hryha, E.; Persson, M.; Bordia, R.K. Analytical models for initial and intermediate stages of sintering of additively manufactured stainless steel. *Acta Mater.* **2023**, *249*, 118822. [CrossRef]

3. Lecis, N.; Beltrami, R.; Mariani, M.; Lecis, N.; Beltrami, R.; Mariani, M. Binder jetting 3D printing of 316 stainless steel: Influence of process parameters on microstructural and mechanical properties. *Metall. Ital.* **2021**, *113*, 31–41.

4. Mostafaei, A.; Stevens, E.L.; Ference, J.J.; Schmidt, D.E.; Chmielus, M. Binder jetting of a complex-shaped metal partial denture framework. *Addit. Manuf.* **2018**, *21*, 63–68. [CrossRef]

5. Cocchi, L.; Mariani, M.; Graziosi, S.; Viganò, R.; Lecis, N. Design challenges in leveraging binder jetting technology to innovate the medical instrument field. *Proc. Des. Soc.* **2024**, *4*, 1737–1746. [CrossRef]

6. Zago, M.; Lecis, N.; Mariani, M.; Cristofolini, I. Analysis of the causes determining dimensional and geometrical errors in 316L and 17-4PH stainless steel parts fabricated by metal binder jetting. *Int. J. Adv. Manuf. Technol.* **2024**, *132*, 835–851. [CrossRef]

7. Alsalla, H.H.; Smith, C.; Hao, L. Effect of build orientation on the surface quality, microstructure and mechanical properties of selective laser melting 316L stainless steel. *Rapid Prototyp. J.* **2018**, *24*, 9–17. [CrossRef]

8. Mao, Y.; Li, J.; Li, W.; Cai, D.; Wei, Q. Binder jetting additive manufacturing of 316L stainless-steel green parts with high strength and low binder content: Binder preparation and process optimization. *J. Mater. Process. Technol.* **2021**, *291*, 117020. [CrossRef]

9. Chen, L.; Chen, W.; Fu, Z.; Ding, G.; Chen, Z.; Zhu, D. Binder Jet 3D Printing of 316L Stainless Steel: Orthogonal Printing and Sintering Process Optimization. *Adv. Eng. Mater.* **2023**, *25*, 2200641. [CrossRef]

10. Grizzle, A.C.; Elliott, A.; Klein, K.L.; Tyagi, P. Surface Finishing and Coating Parameters Impact on Additively Manufactured Binder-Jetted Steel–Bronze Composites. *Materials.* **2024**, *17*, 598. [CrossRef]

11. Jamalkhani, M.; Nathan, B.; Heim, M.; Nelson, D.; Mostafaei, A. Fatigue behavior of vacuum-sintered binder jetted fine 316L stainless steel powder. *Mater. Sci. Eng. A* **2023**, *873*, 144937. [CrossRef]

12. Mostafaei, A.; Neelapu, S.H.V.R.; Kisailus, C.; Nath, L.M.; Jacobs, T.D.B.B.; Chmielus, M. Characterizing surface finish and fatigue behavior in binder-jet 3D-printed nickel-based superalloy 625. *Addit. Manuf.* **2018**, *24*, 200–209. [CrossRef]

13. Chen, H.; Zhao, Y.F. Process parameters optimization for improving surface quality and manufacturing accuracy of binder jetting additive manufacturing process. *Rapid Prototyp. J.* **2016**, *22*, 527–538. [CrossRef]

14. Jamal, M.; Morgan, M. Design Process Control for Improved Surface Finish of Metal Additive Manufactured Parts of Complex Build Geometry. *Inventions* **2017**, *2*, 36. [CrossRef]

15. Fan, F.; Jalui, S.; Manogharan, G. Mass finishing of additively manufactured Ti6Al4V parts: An investigation of surface finish dependency on build orientation and processing conditions. *Manuf. Lett.* **2023**, *35*, 439–449. [CrossRef]

16. Atzeni, E.; Balestrucci, A.; Catalano, A.R.; Iuliano, L.; Priarone, P.C.; Salmi, A.; Settineri, L. Performance assessment of a vibro-finishing technology for additively manufactured components. *Procedia CIRP.* **2020**, *88*, 427–432. [CrossRef]

17. Han, W.; Fang, F. Fundamental aspects and recent developments in electropolishing. *Int. J. Mach. Tools Manuf.* **2019**, *139*, 1–23. [CrossRef]

18. Lee, C.-Y.; Ger, M.-D.; Hung, J.-C.; Yang, P.-J.; Ferng, Y.-C.; Jen, K.-K.; Jian, S.-Y. Effect of phosphoric acid and perchloric acid on Electropolishing of additive manufactured 17-4 PH stainless steel and its characterization. *Int. J. Electrochem. Sci.* **2022**, *17*, 220315. [CrossRef]

19. Yang, G.; Wang, B.; Tawfiq, K.; Wei, H.; Zhou, S.; Chen, G. Electropolishing of surfaces: Theory and applications. *Surf. Eng.* **2017**, *33*, 149–166. [CrossRef]

20. Proskurovsky, D.I.; Rotshtein, V.P.; Ozur, G.E. Use of low-energy, high-current electron beams for surface treatment of materials. *Surf. Coatings Technol.* **1997**, *96*, 117–122. [CrossRef]

21. Zou, J.X.; Zhang, K.M.; Hao, S.Z.; Dong, C.; Grosdidier, T. Mechanisms of hardening, wear and corrosion improvement of 316L stainless steel by low energy high current pulsed electron beam surface treatment. *Thin Solid Films* **2010**, *519*, 1404–1415. [CrossRef]

22. Zhang, K.M.; Zou, J.X.; Bolle, B.; Grosdidier, T. Evolution of residual stress states in surface layers of an AISI D2 steel treated by low energy high current pulsed electron beam. *Vacuum* **2013**, *87*, 60–68. [CrossRef]

23. Huber, D.; Vogel, L.; Fischer, A. The effects of sintering temperature and hold time on densification, mechanical properties and microstructural characteristics of binder jet 3D printed 17-4 PH stainless steel. *Addit. Manuf.* **2021**, *46*, 102114. [CrossRef]

24. *ASTM A564/A564M-19a*; Standard Specification for Hot-Rolled and Cold-Finished Age-Hardening Stainless Steel. ASTM International: West Conshohocken, PA, USA, 2019; pp. 1–8.

25. Emanuelli, L.; Segata, G.; Perina, M.; Regolini, M.; Nicchiotti, V.; Molinari, A. Study of microstructure and mechanical properties of 17-4 PH stainless steel produced via Binder Jetting. *Powder Metall.* **2023**, *66*, 377–386. [CrossRef]

26. Radhakrishnan, J.; Kumar, P.; Gan, S.S.; Bryl, A.; McKinnell, J.; Ramamurty, U. Microstructure and tensile properties of binder jet printed 17–4 precipitation hardened martensitic stainless steel. *Mater. Sci. Eng. A* **2022**, *860*, 144270. [CrossRef]

27. Nezhadfar, P.D.; Verquin, B.; Lefebvre, F.; Reynaud, C.; Robert, M.; Shamsaei, N. Effect of Heat Treatment on the Tensile Behavior of 17-4 PH Stainless Steel Additively Manufactured by Metal Binder Jetting. In Proceedings of the 32nd Annual International Solid Freeform Fabrication (SFF) Symposium, Austin, TX, USA, 2–4 August 2021; pp. 879–890.

28. *ISO 21920-2:2022-12*; Geometrical Product Specifications (GPS)-Surface Texture: Profile—Part 2: Terms, Definitions and Surface Texture Parameters (ISO 21920-2:2021, Corrected Version 2022-06). International Organization for Standardization: Geneva, Switzerland, 2022.

29. Rafi, H.K.; Pal, D.; Patil, N.; Starr, T.L.; Stucker, B.E. Microstructure and Mechanical Behavior of 17-4 Precipitation Hardenable Steel Processed by Selective Laser Melting. *J. Mater. Eng. Perform.* **2014**, *23*, 4421–4428. [CrossRef]

30. Yeli, G.; Auger, M.A.; Wilford, K.; Smith, G.D.W.; Bagot, P.A.J.; Moody, M.P. Sequential nucleation of phases in a 17-4PH steel: Microstructural characterisation and mechanical properties. *Acta Mater.* **2017**, *125*, 38–49. [CrossRef]

31. Mirzadeh, H.; Najafizadeh, A. Aging kinetics of 17-4 PH stainless steel. *Mater. Chem. Phys.* **2009**, *116*, 119–124. [CrossRef]

32. Hsiao, C.N.; Chiou, C.S.; Yang, J.R. Aging reactions in a 17-4 PH stainless steel. *Mater. Chem. Phys.* **2002**, *74*, 134–142. [CrossRef]